Korean J. Chem. Eng., 40(10), 2442-2454 (2023)
DOI: 10.1007/s11814-023-1466-3

pISSN: 0256-1115
eISSN: 1975-7220

Activated carbons derived from polyethylene terephthalate for coin-cell supercapacitor electrodes

Meenkyoung Jung*, Inchan Yang, Dalsu Choi*, Joongwon Lee***,†, and Ji Chul Jung*,†**

*Department of Chemical Engineering, Myongji University, Yongin 17058, Korea
**Institute of Advanced Composite Materials, Korea Institute of Science and Technology, Wanju-gun, Jeollabuk-do 55324, Korea
***Lotte Chemical Research Institute, Daejeon 34110, Korea
(*Received 4 January 2023 • Revised 15 March 2023 • Accepted 7 April 2023*)

Abstract−We successfully prepared activated carbon derived from polyethylene terephthalate (PET) via carbonization and subsequent activation under various conditions and applied it as active material for supercapacitors. In the activation, we used CO_2 for physical activation or KOH for chemical activation and varied the activation temperature from 600 °C to 1,000 °C. We found that CO_2 activation is unsuitable because of insufficient pore formation or low activation yield. Interestingly, PET-derived activated carbon obtained using KOH (PETK) at 700 °C-900 °C exhibited higher specific surface areas than YP50f, which is a commercial activated carbon. Furthermore, some PETKs even displayed a dramatic increase in crystallinity. In particular, the PET-derived activated carbon prepared at 900 °C with KOH (PETK900) had the highest retention rate at a high charge-discharge rate and better durability after 2500 cycles than YP50f. Furthermore, employing the same process that we used with the PET chips, we successfully converted waste PET bottles into activated carbon materials. Waste PET-derived activated carbons exhibited good electrochemical performance as active material for supercapacitors. We thus found chemical activation with KOH to be an appropriate method for manufacturing PET-derived activated carbon and PETKs derived both from PET chips and waste PET have considerable potential for commercial use as active materials for supercapacitors.

Keywords: Polyethylene Terephthalate, Activated Carbon, Plastic Upcycling, Supercapacitor, Organic Electrolyte

INTRODUCTION

Electrical energy storage devices are being researched as an efficient way to store electrical energy. Supercapacitors are one such type of device, and because of their many advantages, including high power density, durable life cycles, and fast discharge rate, they are frequently used in supplementing Li-ion batteries [1-5]. The benefits of supercapacitors can be attributed to their operating principle, which involves the adsorption-desorption of electrolyte ions on the surfaces of electrodes, also known as charge separation in the Helmholtz double layer [1-3]. Owing to these advantages, supercapacitors have been widely used in various applications that require high power density [6,7]. However, supercapacitors have a crucial deficiency: relatively low energy density. Therefore, many researchers have attempted to improve the electrochemical performance of supercapacitors, and developing supercapacitors with high power density and energy density is a mainstream area of research [8-12].

Generally, electrode materials for supercapacitors comprise an active material, a conducting additive, and a binder [13-19]. Porous carbon, which has a large specific surface area (SSA), is frequently used as an active material for supercapacitors to maximize the number of adsorbed electrolyte ions. Owing to its high conductivity and fine powder structure, which can improve the connection between the particles of an active material, carbon black is generally used as a conducting additive for supercapacitors. Generally, two types of binders exist: aqueous type and organic type. Examples of an aqueous binder and an organic binder are polytetrafluoroethylene (PTFE) and polyvinylidene fluoride (PVDF), respectively. The electrochemical properties of supercapacitors are determined by the interactions between the electrode materials. In particular, the active material considerably affects the electrochemical performance of a supercapacitor [20-27].

Activated carbon (AC) is a porous carbon material with a large SSA with a microporous structure [27,28]. It is generally manufactured through carbonization and activation, and the large SSA can be attributed to the formation of pores during the activation process. The properties of AC are determined by the preparation conditions, including the starting materials, carbonization methods, and activation methods. Therefore, depending on the intended field of application, several researchers have manufactured AC with various physical properties under diverse manufacturing conditions. In addition, the cost of the production process of AC is a crucial factor for commercialization. Therefore, it is important to develop an AC-production process with economic feasibility by reducing the required cost. Research on the production of carbon materials using low-cost starting materials has accordingly received attention as a representative method for cost reduction.

Several papers have described the utilization of waste materials

†To whom correspondence should be addressed.
E-mail: joongwon.lee@lotte.net, jcjung@mju.ac.kr

generated from various fields to prepare carbon materials [29-39]. For example, research based on the utilization of food waste, biomass, and domestic waste has been actively reported. In particular, after the outbreak of COVID-19, ecofriendly treatments of plastic attracted attention because plastic waste has increased considerably [40-43]. Most of the waste plastic is processed into landfills or incinerated, both of which cause various environmental problems. Therefore, the preparation of carbon materials using plastic waste is being studied as a promising method for the pro-environmental and efficient upcycling of plastic [33-38]. Various carbon materials can be produced from different types of plastics. Among them, polyethylene terephthalate (PET) is a representative thermoplastic that has an oxygen-containing functional group and a cyclic structure that enables its direct carbonization [37]. Because of these properties, we considered PET as an appropriate starting material for the simple preparation of carbon materials.

Herein, we describe the manufacturing of AC derived from PET and its use as an electrode material for a coin-cell supercapacitor. The aim of this study was to identify the manufacturing conditions required to produce optimized PET-derived AC for use in a supercapacitor with outstanding performance. We prepared PET-based AC using carbonization and various activation methods and checked the physical properties and crystallinity of the prepared PET-derived AC to determine the effect of activation conditions on its characteristics. Subsequently, we investigated the electrochemical performance of the prepared AC by using it as the active material in a supercapacitor. In addition, we determined the correlation between the physical characteristics of the prepared AC and the electrochemical properties of the supercapacitor. Moreover, we evaluated the applicability of these results to the commercialization of PET-derived ACs by comparing their performance in a supercapacitor with that of the commercially available AC.

MATERIAL AND METHODS

1. Preparation of AC Derived from PET

To manufacture AC derived from PET, we first carbonized commercially available PET chips (Lotte Chemical, Republic of Korea) or water bottles (ICIS, Lotte Chilsung, Republic of Korea) and subsequently activated them in a tube furnace. In the carbonization process, we heat-treated 10 g of PET chips or small pieces of waste PET bottles at 800 °C for 2 h at a nitrogen flow rate of 50 ml min^{-1}. To convert the resulting lump of carbon into fine powder, we crushed the carbonized sample using a ball mill operating at 500 rpm for 2 h. We designate the obtained carbon material as PET800.

To synthesize AC, we activated PET800 in a tube furnace using either carbon dioxide (CO_2) or potassium hydroxide (KOH) as activating agents for physical activation or chemical activation, respectively. In both activation methods, we performed the activation processes at 600 °C-1,000 °C with a heating rate of 5 °C min^{-1}, maintaining the target temperature for 2 h. During physical activation, we fixed the flow rate of CO_2 as 100 ml min^{-1}. Conversely, during chemical activation, we fixed the mass ratio of PET800 to KOH as 1 : 4 and maintained the flow rate of nitrogen as 100 ml min^{-1}. Additionally, we washed the carbon activated using KOH several times with distilled water until the pH became neutral and then dried the samples in a convection oven at 100 °C for 24 h. Herein, we denote the prepared PET-derived AC as PETXY, where X stands for the activating agent (CO_2 (C) or KOH (K)) and Y stands for the activation temperature. Similarly, we designate the carbon material and AC manufactured using waste bottles as PET800(w) and PETXY(w), respectively. For comparison, we purchased YP50f (Kuraray Co., Japan), which is a commercially available AC that is used in supercapacitors. We used and analyzed YP50f as received without further treatment.

2. Characterization of AC Derived from PET

To determine the physical properties, including the SSA, average pore diameter, and pore volume, of the prepared and purchased carbon materials (PET800 and PETXYs and YP50f, respectively), we used a constant-volume adsorption apparatus (BELSORP-Max II, MicrotracBEL, Japan) at 77 K to obtain nitrogen adsorption-desorption isotherm data. In addition, we employed the Brunauer-Emmett-Teller (BET) equation to calculate the SSAs of the prepared and purchased carbon materials [44]. We used Raman spectroscopy (DXP2xi, Thermo, USA) to determine the crystallinity and carbon structure of the prepared and purchased carbon materials. To investigate the morphology of the PET-derived carbon, we performed scanning electron microscopy (SEM) (SU-70, Hitachi, Japan) analysis. We conducted thermal gravimetric analysis (TGAs) using a high-temperature simultaneous thermal analyzer (STA449 F3, NETZSCH, Germany) to determine the thermophysical properties.

3. Fabrication of Supercapacitors

We fabricated coin-cell supercapacitors using the prepared and purchased ACs (PETKs and YP50f, respectively) as the active materials, Super-P (M.M.M. Carbon Co., Belgium) as the conducting additive, and polyvinylidene fluoride (PVDF, Sigma-Aldrich) as the binder, all dissolved in 1-methyl-2-pyrrolidone (NMP, Daejung Chem., Republic of Korea). We fixed the mass ratios of the active material, conducting additive, and binder as 8 : 1 : 1. We mixed the active material and conducting additive via ball milling for 30 min and added the binder to this mixture. To control the viscosity, we added NMP to the mixture and then stirred it for >1 h. We coated the resulting homogeneous slurry onto an aluminum current collector using a doctor blade with a gap of 170 μm. We dried the coated electrodes first in a convection oven and then in a vacuum oven at 70 °C for 24 h each. After drying, we pressed the electrodes at 80 °C using a roll press and punched out circular electrodes of 16-mm diameter. In a glove box filled with argon gas, we fabricated each coin-cell supercapacitor (CR2030) comprising a pair of these electrodes, a separator, and a spacer. We soaked the electrodes in 1-M tetraethylammonium tetrafluoroborate in acetonitrile ($TEABF_4$/ACN, Enchem, Republic of Korea) for 12 h. We positioned the electrodes facing each other, with a separator between them, and sealed the fabricated supercapacitors using a crimper (Wellcos Co., Republic of Korea). The overall supercapacitor fabrication process is presented in Fig. 1.

4. Electrochemical Characterization of Supercapacitors

We performed cyclic voltammetry (CV), galvanostatic charge-discharge (C-D) measurements, and electrochemical impedance spectroscopy (EIS) using an electrochemical workstation (CS310, CorrTest, China). To measure the capacitance of each fabricated supercapacitor, we recorded the CV curves at scan rates of 5-300

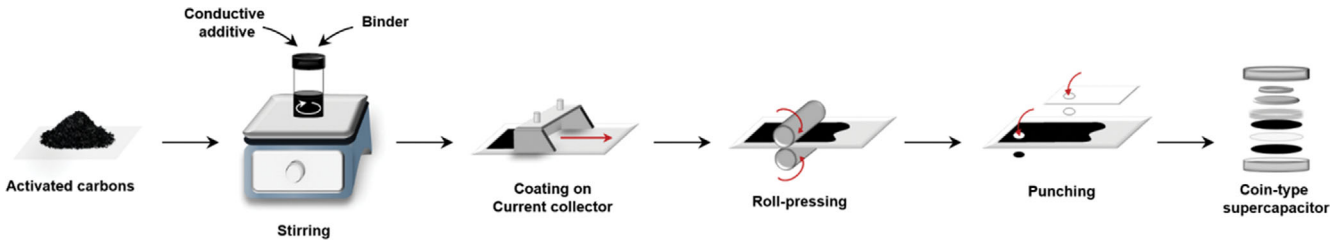

Fig. 1. Scheme of the coin-cell supercapacitor fabrication process.

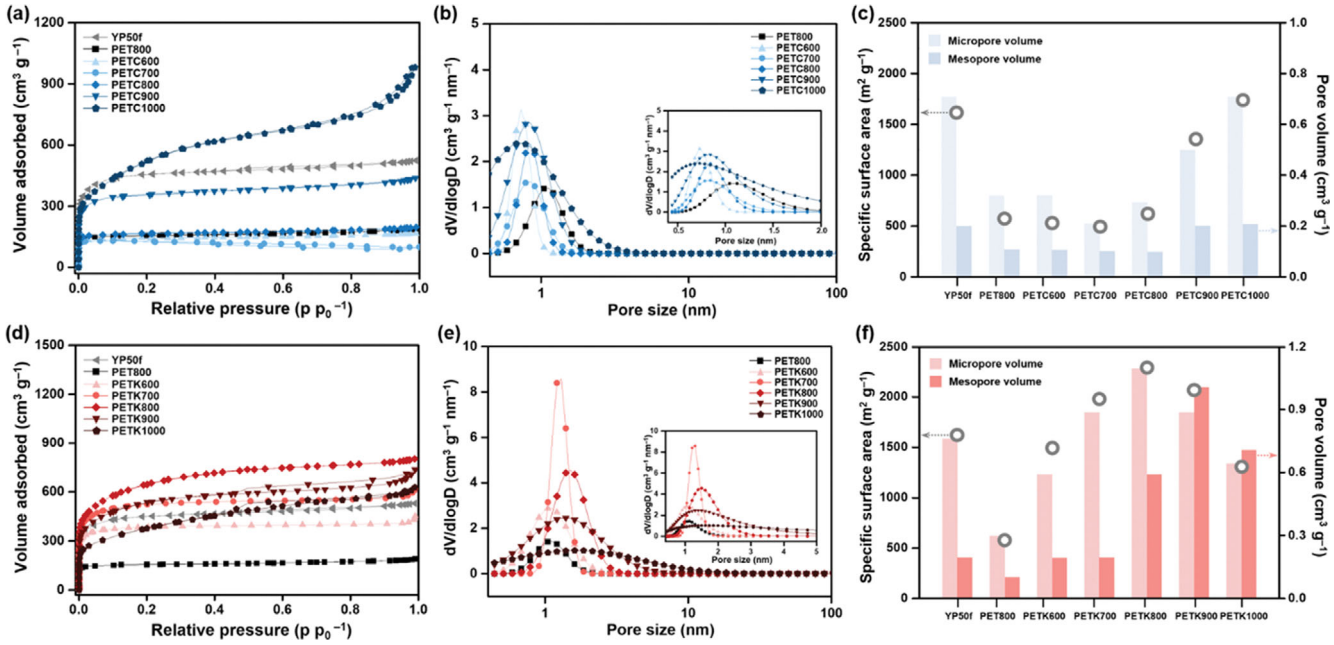

Fig. 2. (a) N_2 adsorption-desorption isotherms of PETCs, (b) pore size distributions of PETCs, (c) pore volumes of PETCs, (d) N_2 adsorption-desorption isotherm of PETKs, (e) pore size distributions of PETKs, and (f) pore volumes of PETKs.

mV s^{-1} in the voltage range of 0-2.7 V. Further, we performed C-D analysis at constant current density (0.1-7 A g^{-1}) in the same voltage range. We calculated the specific capacitance of the supercapacitors using the C-D curves in two ways, obtaining the gravimetric capacitance (C_g) and volumetric capacitance (C_v). Furthermore, we performed 2500 C-D cycles at a current density of 1 A g^{-1} to investigate the long-term durability of the supercapacitors. We performed EIS analysis to observe their resistance behavior and used Nyquist plots to show the results of the EIS measurements over the frequency range of 100 kHz-0.01 Hz. To investigate the resistance of the electrode materials, we additionally performed four-point probe measurements (FPP, CMT-SR1000N, Advanced Instrument Technology).

RESULTS AND DISCUSSION

1. Physical Properties of the PET-derived Carbons

Several previous studies have established that the physical characteristics of the active material considerably affect the performance of a supercapacitor [30,31,45-47]. It is therefore crucial to verify the features of AC, such as its SSA, pore volume, and pore diameter, to utilize it as an active material. Hence, we obtained N_2 adsorption-desorption isotherms of the prepared carbons (YP50f, PET800, and PETXYs), and the results are shown in Fig. 2 and Table 1. To calculate the SSA from these results, we used the BET equation.

We found that PET800, the carbon material manufactured by carbonizing PET chips, exhibits poorly formed pores and a low SSA of 581.1 m^2 g^{-1}. Following the activation procedure, the characteristics of the prepared ACs developed differently depending on the activation conditions used. For the PETCs, which were produced using the physical activation process, we observed no drastic change in the SSA and pore structure at 600 °C-800 °C. However, a substantial increase in the SSA did occur at 900 °C and 1,000 °C. For example, PETC1000 exhibited a large SSA of 1,737.5 m^2 g^{-1}, which is higher than that of YP50f. The formation of micropores in PETC900 and PETC100 is thought to be the main cause for this increase in the SSA. In general, it is known that the development of micropores and mesopores of carbon materials creates a high specific surface area [46]. As shown in Fig. 2, both mesopores and micropores were simultaneously developed in PETKs, whereas only micropores were intensively formed in PETCs during the

Table 1. Physical properties of YP50f and PET-derived carbon

	YP50f	PET800	PETC600	PETC700	PETC800	PETC900	PETC1000	PETK600	PETK700	PETK800	PETK900	PETK1000
S_{BET}[a] [$m^2\ g^{-1}$]	1,631.1	581.1	538.0	495.6	622.3	1,360.0	1,737.5	1,488.4	1,983.8	2,287.8	2,076.7	1,316.8
D_{avg}[b] [nm]	1.9	1.8	1.8	1.8	1.8	1.8	1.7	1.9	1.9	2.0	2.4	3.1
V_{micro}[c] [$cm\ g^{-1}$]	0.7	0.3	0.3	0.2	0.3	0.5	0.7	0.6	0.9	1.1	0.9	0.6
V_{meso}[d] [$cm\ g^{-1}$]	0.2	0.1	0.1	0.1	0.1	0.2	0.2	0.2	0.2	0.6	1.0	0.7
V_{total}[e] [$cm\ g^{-1}$]	0.8	0.3	0.3	0.3	0.3	0.6	0.8	0.7	1.0	1.3	1.1	0.8

[a]Specific surface area. [b]Average pore diameter. [c]Micropore volume. [d]Mesopore volume. [e]Total pore volume.

activation process. Accordingly, we assumed that the high SSA of PETC900 and PETC1000 was attributed to their micropore development.

Interestingly, we observed more remarkable results for the PETKs. We found a considerable increase in the SSA for all the PETKs and PETK800 and PETK900 showed SSAs of 2,287.8 and 2,076.7 $m^2\ g^{-1}$, respectively. Furthermore, in contrast to the PETCs, the pore volumes of the PETKs shown in Fig. 2(f) revealed that the micropores and mesopores in PETKs grew during the chemical activation processes. The detailed analysis of the development of the pore structure and the change in the SSA as functions of the activation temperature showed that the micropore volume increased at activation temperatures of 600 °C-800 °C and decreased at higher temperatures. In addition, we found that the mesopore volume of PETK800 was three times that of PETK700, the mesopore volume of PETK900 increased, and the mesopore volume of PETK1000 declined when compared with that of PETK900.

Based on these changes in physical characteristics with varying activation temperatures, we can understand the formation process of pores during chemical activation of the PET-derived carbon. Micropores were first created actively via chemical activation at 600 °C-800 °C. When the temperature was increased to 900 °C, additional mesopores were formed by the merging of micropores, reducing the number of micropores. At the highest activation temperature of 1,000 °C, excessive activation resulted in the collapse of the pores, decreasing the number of micropores and mesopores. Based on the abundance of micropores, the activation conducted at 800 °C affords the largest SSA, while the activation conducted at 900 °C produced plentiful micropores and mesopores concurrently. Thus, we have verified that the use of appropriate activation conditions is crucial because the physical properties of the resulting carbon material change depending upon the activation temperatures and activating agents [30,46,48].

Both the activation conditions and the acquired yield are crucial for the practical application of the prepared ACs. We therefore calculated the carbonization and activation yields of the PET-derived carbons, and the results are shown in Fig. 3. We calculated the yield of the heat-treatment processes (carbonization and activation) using Eqs. (1) and (2), respectively:

$$y_c = m_c / m_{PET} \times 100\%, \quad (1)$$

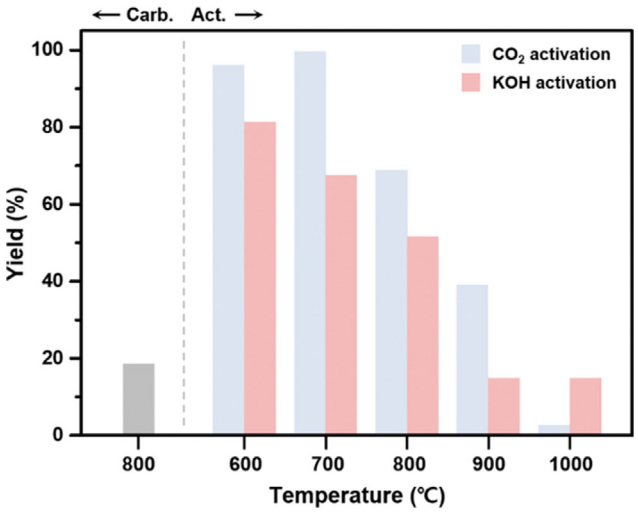

Fig. 3. The yield of PET-derived carbon.

$$y_a = m_a / m_i \times 100\%. \quad (2)$$

Here, y_c denotes the carbonization yield, m_c represents the mass of carbon material obtained after carbonization, and m_{PET} denotes the mass of the PET before carbonization. Similarly, y_a denotes the activation yield, m_a represents the mass of PETXYs obtained after activation, and m_i denotes the mass of the carbonized PET (PET800) before activation. The obtained carbonization yield (y_c) is ~18%, which is comparable to the results reported in several previous papers [33,37,49]. Interestingly, the activation yield is inversely proportional to the activation temperature. We found that the yields of the PETCs decreased more considerably compared with those of the PETKs with increasing activation temperature. Among the prepared PETXYs, PETC1000 showed the lowest activation yield (y_a<3%). Therefore, in spite of its large SSA, PETC1000 is unsuitable for use as an electrode material in a supercapacitor because of its low yield. According to the SSAs and yields, the KOH activations, particularly, at 800 °C and 900 °C are suitable for preparing AC with appropriate physical properties for use as an electrode material in a supercapacitor.

2. Crystallinity and Morphology of the PET-derived Carbons

In addition to its SSA, the crystallinity of a carbon material is an

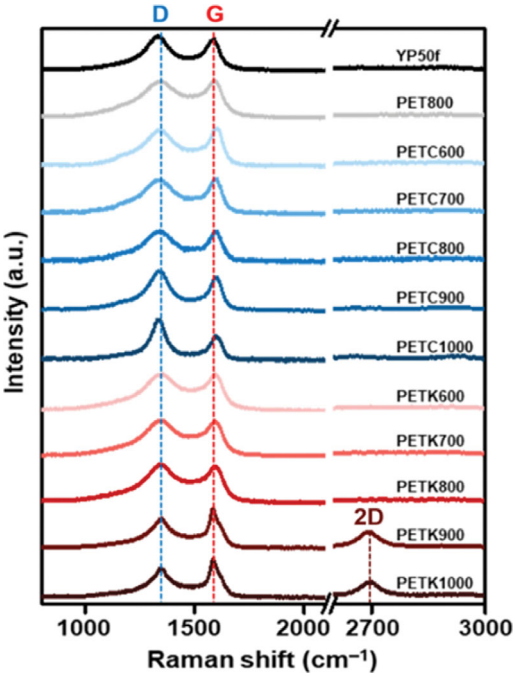

Fig. 4. Raman spectra of YP50f and PET-derived carbons.

essential characteristic for its use as an active material in a supercapacitor. We therefore determined the crystallinity of PETXYs using Raman spectroscopy. The acquired Raman spectra are displayed in Fig. 4, and the corresponding ratios of the intensity of the D peak (≈1,350 cm^{-1}) to that of the G peak (≈1,580 cm^{-1}) are listed in Table 2. In general, we used the I_D/I_G values obtained from the Raman spectra to calculate the lateral size L_a of the crystallites [50-52]. However, two equations can be used to calculate L_a, depending on the degree of graphitization of the sample. For amorphous carbon, the Ferrari-Robertson relation shows that L_a is directly proportional to I_D/I_G. Conversely, for nanocrystalline graphite materials, i.e., when the 2D peak (≈2,710 cm^{-1}) is observed, the two factors are inversely proportional, given by the Tuinstra-Koenig relation [52]. The measured Raman spectra of the prepared PET-derived carbons show that neither PETCs nor PETKs exhibit any noteworthy change in I_D/I_G at 600 °C-800 °C. Conversely, we observed an increase in crystallinity with both activation methods after activation at 900 °C and 1,000 °C. In particular, we observed 2D peaks for PETK900 and PETK1000, suggesting a noticeable increase in crystallinity. By calculating the value of L_a from I_D/I_G using equations, we found that PETK900 and PETK1000 each showed a substantial increase in lateral size. In accordance with our previous studies and other related works, this is attributed to pore formation during the KOH activation processes and the removal of non-graphitic components [30,46,48].

To determine the morphology of the PET-derived carbons directly, we performed SEM analysis. The obtained SEM images of PET800, PETK800, and PETK900 are shown in Fig. 5. As shown in Fig. 5(a), PET800 comprises particles of irregular size and shape. There is no drastic change in morphology after the activation at 600 °C-800 °C. In fact, the SEM image of PETK800 presented in Fig. 5(b) shows a morphology that is comparable to that of PET800. Meanwhile, the morphology of PETK900, which has a well-developed crystalline structure, shows that merging between the particles has formed bulky lumps. This result is attributed to the aggregation between basic domains during KOH activation at high temperatures [46]. Accordingly, we expected PETK900 to be a potential electrode material for use in supercapacitors owing to its large SSA and high crystallinity.

3. Electrochemical Properties of the Fabricated Supercapacitors

3-1. Capacitance Properties

Based on the physical properties and crystallinity of the PET-based ACs described above, PETK600, PETK700, PETK800, and PETK900, in which relatively large SSAs were observed, were applied as electrode materials in a supercapacitor, and their electrochemical characteristics were analyzed. For comparison, we performed concurrent electrochemical-characteristic analysis using YP50f to investigate the possibility of commercializing the PET-derived carbons.

To evaluate the electrochemical properties of supercapacitors

Table 2. Intensity ratios of the D peak to the G peak in Raman spectra and the crystallite size (L_a) of YP50f and PET-derived carbons

	YP50f	PET800	PETC600	PETC700	PETC800	PETC900	PETC1000	PETK600	PETK700	PETK800	PETK900	PETK1000
I_D/I_G	1.10	0.97	0.94	0.97	1.01	1.18	1.70	0.99	1.02	1.04	0.74	0.74
L_a [nm]	0.24	0.22	0.22	0.22	0.23	0.25	0.30	0.23	0.23	0.23	25.97	25.81

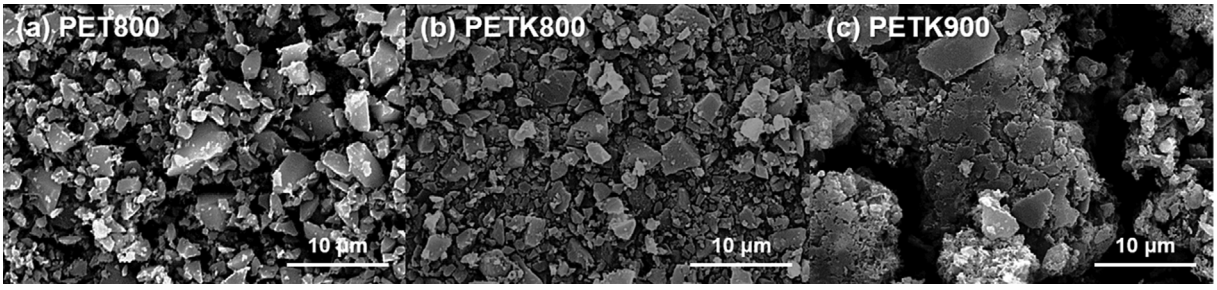

Fig. 5. SEM images of (a) PET800, (b) PETK800, and (c) PETK900.

Table 3. Thickness and loading mass of electrodes using YP50f and PETK samples

	YP50f	PETK600	PETK700	PETK800	PETK900
Thickness [μm]	68	67	65	75	70
Loading mass [mg cm^{-2}]	5.1	4.6	4.2	5.8	4.6

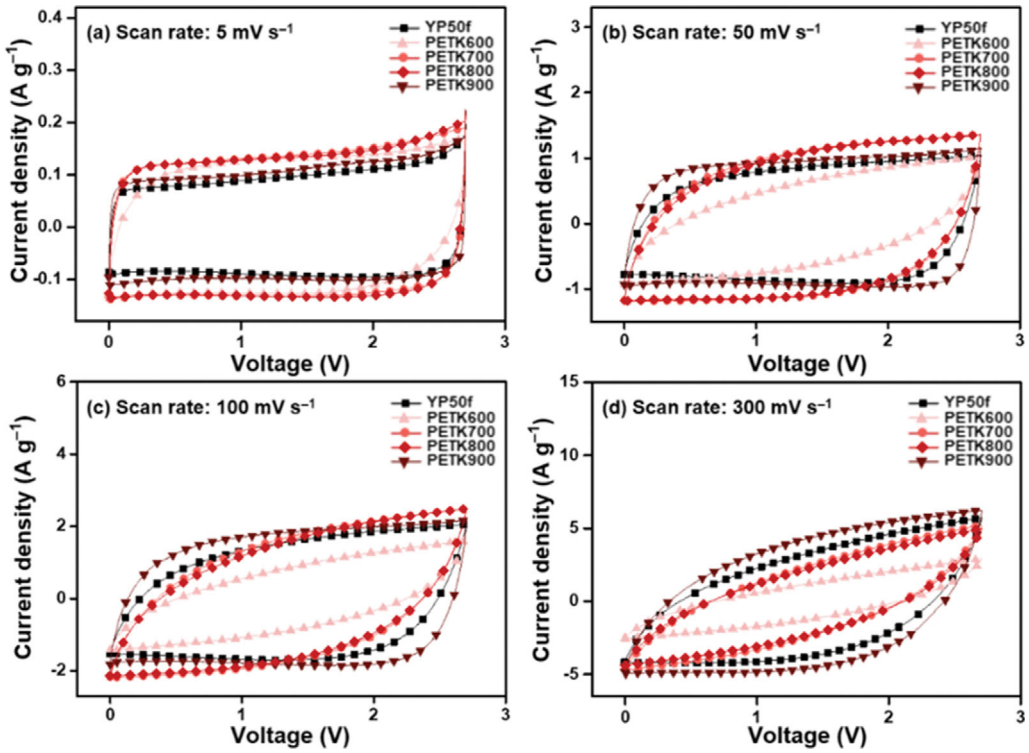

Fig. 6. Cyclic voltammograms of supercapacitors using YP50f and PETKs at scan rates of 5 mV s^{-1}, 50 mV s^{-1}, 100 mV s^{-1}, and 300 mV s^{-1}.

with PETKs and YP50f, we conducted electrochemical characterization using CV, C-D, EIS, and FPP. For these studies, we used an organic electrolyte ($TEABF_4$/ACN) and a two-electrode system (2E) that is considered to be more industrially appropriate. Before discussing the electrochemical properties, we first address some of the distinctions between the 2E and three-electrode system (3E) [53]. Eq. (3) is generally used to define the relation between the 2E and 3E capacitances, where C_{3E} and C_{2E} are the capacitances determined from the 3E and the 2E system, respectively:

$$C_{3E}=4\times C_{2E}. \quad (3)$$

Table 3 presents the thicknesses and loading masses of the prepared carbon electrodes. To directly investigate the capacitance, we obtained cyclic voltammograms of the fabricated supercapacitors at the scan rates of 5, 50, 100, and 300 mV s^{-1}, and the results are shown in Fig. 6. At the lowest scan rate of 5 mV s^{-1}, the cyclic voltammograms of all the supercapacitors exhibited rectangular CV curves. However, as we increased the scan rate to 300 mV s^{-1}, the CV curves transformed into rugby-ball shapes. As reported in previous studies, this occurs because the SSA of an active material substantially affects the capacitance of the supercapacitor at a low scan rate, while the electrical conductivity of the carbon electrodes considerably influences the retention rate at a high scan rate. For comparison, we calculated the gravimetric capacitances of the fabricated supercapacitors from these cyclic voltammograms using Eq. (4), and the results are shown in Table 4.

$$C=\frac{I_a+|I_c|}{2m\times(dV/dt)}. \quad (4)$$

Here C denotes the specific capacitance, I_a and I_c represent the anodic current and cathodic current, respectively, m denotes the

Table 4. Specific capacitances of supercapacitors using YP50f and PETKs, as calculated from cyclic voltammograms

	Gravimetric capacitance [F g^{-1}]					
Scan rate [mV s^{-1}]	5	10	30	50	100	300
YP50f	18.4	17.6	16.0	14.9	13.0	8.9
PETK600	22.8	20.0	13.4	10.2	6.8	3.1
PETK700	25.9	24.3	20.7	18.0	13.3	6.0
PETK800	25.8	24.2	20.4	17.6	12.7	5.7
PETK900	20.8	19.9	18.4	17.6	15.9	11.4

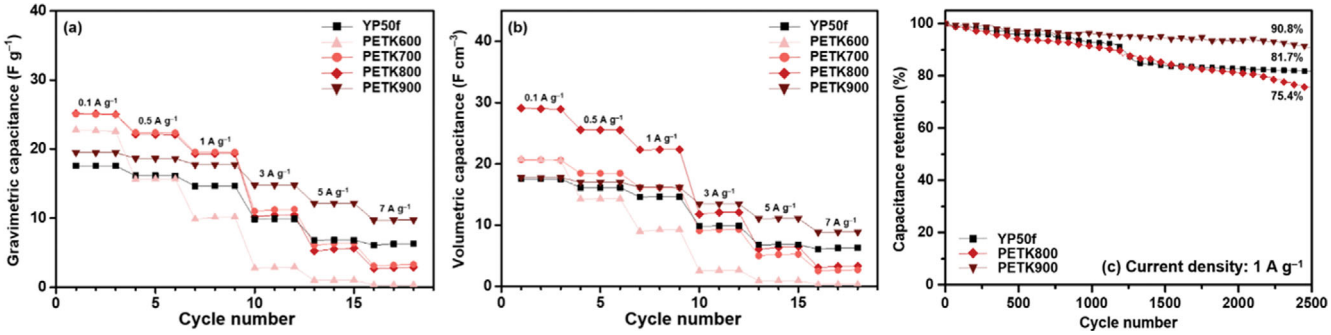

Fig. 7. (a) Gravimetric capacitances, (b) Volumetric capacitances, and (c) long-term durability of supercapacitors using YP50f and PETKs.

Table 5. Specific capacitances of supercapacitors using YP50f and PETKs

Current density [A g^{-1}]	Gravimetric capacitance [F g^{-1}]						Volumetric capacitance [F cm^{-3}]						R_{ret} [a] [%]
	0.1	0.5	1	3	5	7	0.1	0.5	1	3	5	7	
YP50f	17.6	16.1	14.6	9.9	6.8	6.3	17.5	16.1	16.4	9.9	6.8	6.3	35.8
PETK600	22.6	15.7	10.2	2.9	1.0	0.4	20.6	14.3	9.3	2.7	0.9	0.3	1.8
PETK700	25.0	22.4	19.6	11.2	6.4	3.3	20.6	18.5	16.1	9.3	5.3	2.7	13.2
PETK800	25.0	22.1	19.3	10.5	5.6	2.9	28.9	25.5	22.3	12.1	6.5	3.3	11.6
PETK900	19.5	18.6	17.7	14.8	12.2	9.7	17.8	17.0	16.1	13.5	11.1	8.9	49.7

[a]Retention ratio with increasing C-D; calculated from the ratio of specific capacitances at 0.1 and 7 A g^{-1}.

total weight of active material of the two electrodes, and dV/dt represents the scan rate.

At the scan rate of 5 mV s^{-1}, all the supercapacitors using the PETKs exhibit higher capacitances than that of the supercapacitor using YP50f. In particular, PETK800 exhibits a high capacitance because it has the largest SSA. At 300 mV s^{-1}, the highest scan rate, we found that except for PETK900, most of the PETKs could not maintain their initial capacitance values. However, PETK900 maintained its capacitance well, as expected, because of its well-developed crystallinity. We found that PETK900 outperformed YP50f at all scan rates.

In addition, to verify the capacitance property, we performed C-D analysis at the current densities of 0.1, 0.5, 1, 3, 5, and 7 A g^{-1}, and the results are shown in Fig. 7. We calculated the specific capacitances (C_g and C_v) of the supercapacitors using Eqs. (5) and (6):

$$C_g = \frac{I \times \Delta t}{m \times \Delta V}, \quad (5)$$

$$C_v = C_g \times \rho_{electrode}, \quad (6)$$

where C_g and C_v denote the gravimetric capacitance and volumetric capacitance, respectively, I represents the discharge current, Δt denotes the discharge time, m represents the total weight of the active material in the two electrodes, ΔV denotes the voltage change during the discharge process, and $\rho_{electrode}$ is determined from the ratio of the loading mass of the active material to the volume of the electrode. Additionally, we calculated the retention ratio (R_{ret}), which is the ratio of the specific capacitance at 0.1 A g^{-1} to that at 7 A g^{-1}, to determine the rate capabilities of the supercapacitors. The specific capacitances and R_{ret} determined from the C-D results are presented in Table 5.

The results of the C-D measurements are comparable to those of the CV measurements. The gravimetric capacitances of all the supercapacitors fabricated using the prepared ACs at 0.1 A g^{-1}, the lowest current density, exhibited higher values than that using YP50f. However, the volumetric capacitances have different tendencies from the gravimetric capacitances because the loading mass changes according to the properties of the carbon materials. Thus, as discussed above, we found that PETK900, which exhibited both a large SSA and high crystallinity, has a higher gravimetric capacitance than that of the supercapacitor using YP50f under all the measurement conditions and an outstanding retention rate of 49.7%. Although various factors, such as crystallinity, pore structure, and particle connectivity of carbon electrode, could affect the retention rate of supercapacitors, we assume that the excellent retention rate of PETK900 is mainly due to its high crystallinity. Moreover, we performed 2500 cycle tests of the supercapacitors fabricated using PETK800, PETK900, and YP50f to evaluate their long-term durability, and the results are shown in Fig. 7(c). For 2500 cycles, YP50f preserved 81.7% of the initial capacitance, while PETK800 and PETK900 demonstrated long-term durability of 75.4% and 90.8%, respectively. In order to confirm the excellent performance of the PET-derived activated carbons, Ragone plots of YP50f, PETK800 and PETK900 obtained from the C-D results are displayed in Fig. S1. The energy density (E) and power density (P) were calculated using Eqs. (S1) and (S2), respectively. In particular, PETK900 showed higher energy and power density than YP50f in all the evaluation conditions, indicating that PET-derived activated carbons can be promising materials as supercapacitor electrode.

Under the same conditions as described above, we also per-

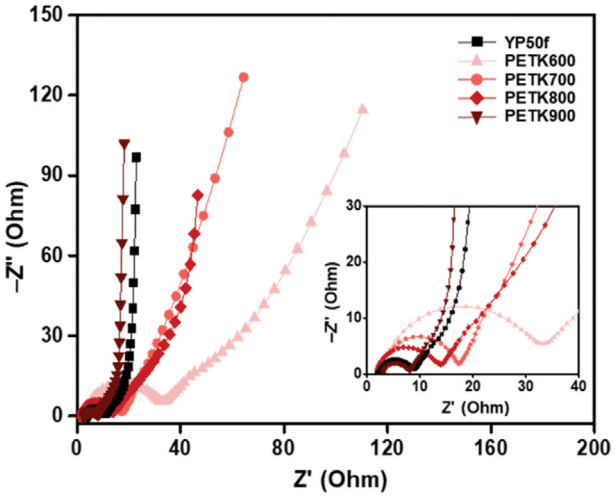

Fig. 8. Electrochemical impedance spectra of supercapacitors using YP50f and PETKs. The inset shows an expanded view of the region near the origin.

formed electrochemical characterizations of a supercapacitor fabricated using PETC900 (Fig. S2), which showed a slight increase in the SSA among the PETCs. The specific capacitances calculated from the CV and C-D results are presented in Tables S1 and S2, respectively. Owing to its unchanged morphology and inadequate SSA development, PETC900 displayed lower capacitance under all measurement conditions than YP50f.

3-2. Resistance Properties

To evaluate the electrical resistance properties of the supercapacitors, we performed EIS analysis, and the results are shown using the Nyquist plot in Fig. 8. In general, Nyquist plots have three parts: bulk-solution resistance, charge-transfer resistance, and Warburg resistance [54-58]. The bulk-solution resistance due to the electrolyte ions is observed in the high-frequency region on the x axis, i.e., the real part of the impedance. The charge-transfer resistance (R_{ct}), which is observed in the middle-frequency region, appears in the form of a semicircle. R_{ct} includes the electrolyte resistance in the pores of the electrodes and the contact resistance between the electrode and current collector. Thus, R_{ct} functions as a crucial component in determining the resistance characteristics of the supercapacitor. The Warburg region is a nonvertical line that is located before the long straight line in the low-frequency region; it is attributed to the limitation of ionic transport or a nonuniform pathway for ion transfer. The capacitive behavior of the electric double layer generated at the interface between the electrode and electrolyte is expressed in the form of a vertical line.

In Fig. 8, R_{ct}, indicated by a semicircle, displays a strong connection to the rate capability obtained from the C-D results. Among the fabricated supercapacitors, the supercapacitor using PETK600, which has the lowest retention rate, exhibits the largest semicircle diameter. The supercapacitors using YP50f and PETK900, which have relatively high retention rates, exhibit smaller semicircle diameters than the others. Based on its high electrical conductivity, an electrode material with a low R_{ct} is demonstrated to be crucial for a high retention rate. In addition, we performed FPP analysis to analyze the resistance properties of only the electrode material (Table 6). The resistance characteristics exhibited in the Nyquist plots and the FPP results tend to be similar. When comparing the EIS and FPP results, PETK600, which exhibited the largest R_{ct}, had the highest sheet resistance of 2,064 Ohm sq.$^{-1}$. Conversely, PETK900, which exhibited the smallest R_{ct}, had the lowest sheet resistance of 249 Ohm sq.$^{-1}$. These results show that the resistance of the electrode material considerably affects the resistance of the supercapacitor. In conclusion, PETK900 exhibits superb performance, including low resistance and outstanding capacitance, based on the high electrical conductivity owing to its exceptional crystallinity and the ease of transferring electrolyte ions from its abundant mesopores.

In addition, the EIS analysis, which verifies the resistance characteristics of PETC900 [Fig. S1(c)], further confirms the correlation between the retention rate and R_{ct} represented by the semicircle in the Nyquist plot. The EIS result for PETC900 shows a small-diameter semicircle because PETC900 has a higher retention rate than any of the PETKs, with the exception of PETK900. This can be attributed to a slight increase in crystallinity, as observed in Raman spectroscopy. However, PETC900 exhibits a higher Warburg resistance than YP50f owing to its lack of pore formation under the inadequate activation conditions.

4. Thermal and Physical Properties of the Waste PET-derived Carbons

To apply the process for manufacturing PET-derived ACs to actual plastic waste, we selected waste PET bottles as a starting material for preparing the waste PET-derived ACs. Because waste PET bottles account for a considerable amount of plastic waste, they are directly collected and used for recycling [35]. To examine the applicability of the aforementioned activation method, we recycled this waste PET by converting the PET bottles into AC under the same conditions as described above. Because thermal properties are the crucial factor in converting PET into carbon material, we performed TGAs of waste PET bottles and PET chips under two conditions, and the results are shown in Fig. 9. In both samples, weight loss was observed in two steps under air condition, but in one step under nitrogen condition. As expected, 15% of the final residue remained under nitrogen condition, while nothing remained due to the complete combustion of carbon material under air condition. It is noteworthy that the waste PET and the PET chips show similar thermal properties in both conditions. Therefore, we expect that carbon materials produced from both PET materials would exhibit similar physical and chemical properties.

Table 6. Sheet resistances of YP50f and PETKs

	YP50f	PETK600	PETK700	PETK800	PETK900
R_{sheet}[a] [Ohm sq.$^{-1}$]	843	2,064	873	667	249

[a]Sheet resistance

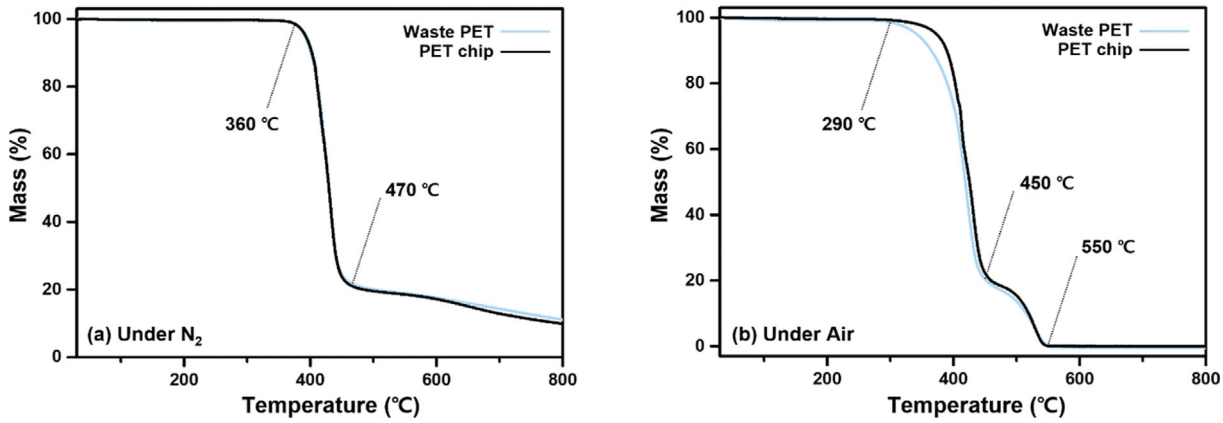

Fig. 9. TGA data for waste PET and PET chips obtained in (a) nitrogen and (b) air.

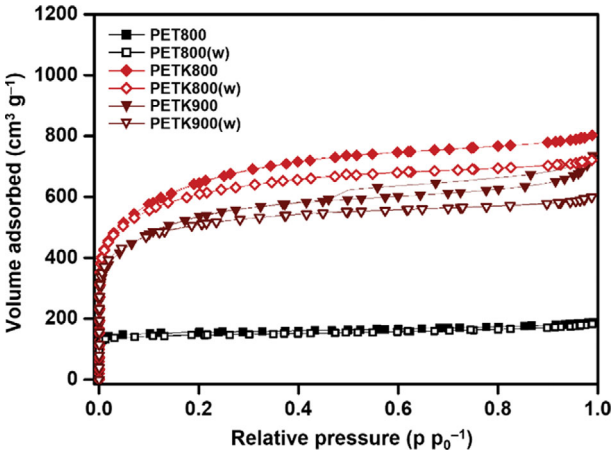

Fig. 10. N_2 adsorption-desorption isotherms of waste-PET-derived carbons.

We synthesized the waste PET-derived ACs using the same carbonization and activation processes as described above. We used the following two activation conditions: KOH activation at 800 °C, which showed the largest increase in SSA, and KOH activation at 900 °C, which exhibited the greatest development in crystallinity. To determine the SSAs and pore structures of these waste PET-derived carbons, we obtained N_2 adsorption-desorption isotherms for PET800(w), PETK800(w), and PETK900(w). As shown in Fig. 10 and Table 7, similar SSA values and isotherms were observed for the carbon materials prepared under the same conditions [compared with Table 1 and Fig. 2(d)]. However, compared with the carbon material obtained from PET chips, the carbon material derived from waste PET had a slightly lower SSA. Furthermore, we did not observe the hysteresis shown by PETK900 in PETK900(w), indicating that waste PET-derived AC has less pore structure development. For comparison, SSAs and pore volumes of PETK800(w) and PETK900(w) are presented in Fig. S3.

Table 7. Specific surface areas of PET800(w), PETK800(w), and PETK900(w)

	PET800(w)	PETK800(w)	PETK900(w)
S_{BET} [$m^2\ g^{-1}$]	581.2	2,174.7	1,891.4

As shown in Fig. 11, we analyzed the morphology of the waste PET-derived carbon. Similar to the carbon generated from PET chips, we observed no noticeable change in the morphology between PET800(w) and PETK800(w). Meanwhile, although PETK900(w) showed aggregation among particles in the similar manner as observed for PETK900, it clumped less than PETK900. Therefore, we predict that the electrical conductivity of PETK900(w) will be lower than that of PETK900. However, we found that carbon materials generated from waste PET and PET chips generally have comparable physical properties. Therefore, the method we have employed can be used for the recycling of waste PET.

5. Electrochemical Properties of the Supercapacitors Using Waste PET-derived Carbons

5-1. Capacitance Properties

To evaluate the electrochemical properties of the waste PET-derived carbons, we fabricated supercapacitors using PETK800(w)

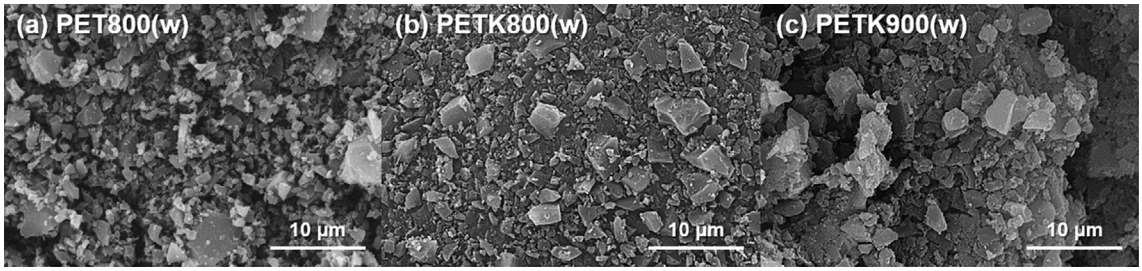

Fig. 11. SEM images of (a) PET800(w), (b) PETK800(w), and (c) PETK900(w).

Table 8. Thickness and loading mass of electrodes using PETK800(w) and PETK900(w)

Sample	PETK800(w)	PETK900(w)
Thickness [μm]	70	65
Loading mass [mg cm^{-2}]	5.1	4.2

Table 9. Specific capacitances of supercapacitors PETK800(w) and PETK900(w) calculated from cyclic voltammograms

	Gravimetric capacitance [F g^{-1}]					
Scan rate [mV s^{-1}]	5	10	30	50	100	300
PETK800(w)	23.4	21.2	20.5	18.5	14.7	7.9
PETK900(w)	21.0	20.4	17.2	16.9	15.6	11.7

and PETK900(w). The thicknesses and loading masses of the electrodes have similar values to those of the electrodes fabricated using PET chip-derived AC, and the results are presented in Table 8 (compared with Table 3).

After fabricating the supercapacitors, we performed their electrochemical analysis under the same conditions as described previously. For comparison, we recorded cyclic voltammograms of the supercapacitors fabricated using PETK800(w) and PETK900(w) at the same scan rates of 5, 50, 100, and 300 mV s^{-1} (Fig. 12; compared with Fig. 6). To calculate the specific capacitances, we used Eq. (4), and the values are presented in Table 9 (compared with Table 4). When comparing the cyclic voltammograms of the supercapacitors fabricated using each type of PET-derived ACs at 5 mV s^{-1}, PETK800(w) and PETK900(w) show capacitances similar to those of PETK800 and PETK900, respectively. Interestingly, PETK800(w) and PETK900(w) considerably maintained their initial capacitance with an increase in the scan rate. Consequently, at the greatest scan rate, PETKs(w) exhibit higher capacitances than PETKs.

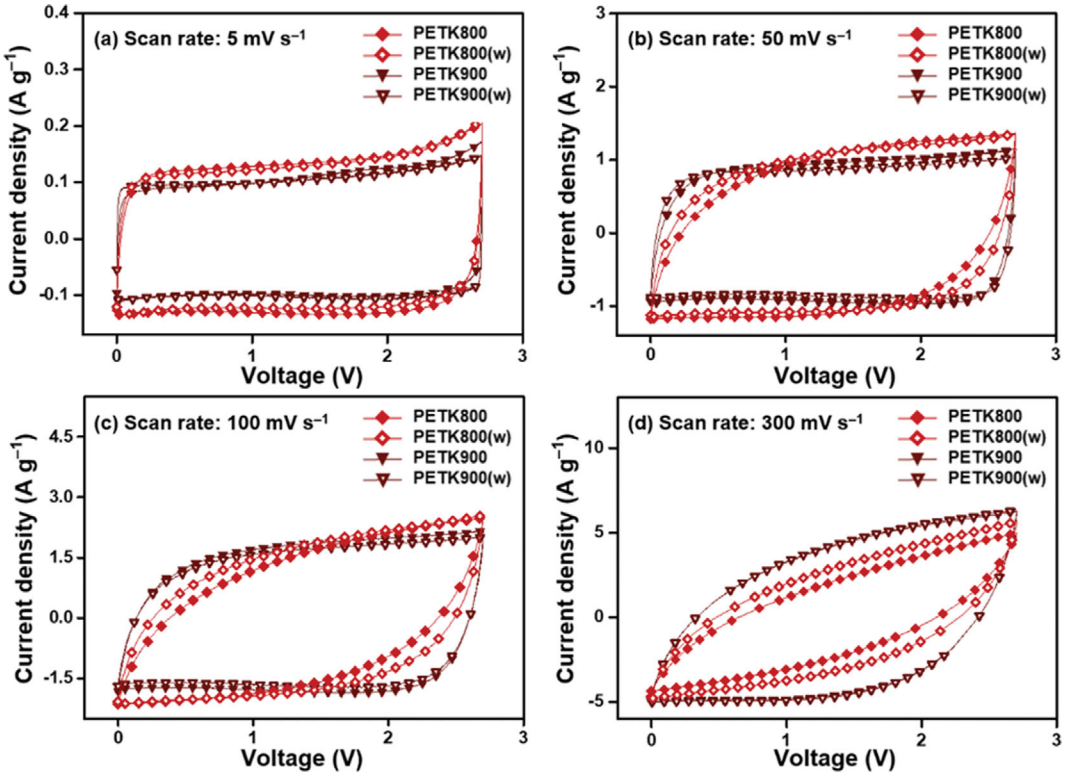

Fig. 12. Cyclic voltammograms of supercapacitors using PETK800s and PETK900s derived from waste PET or from PET chips at scan rates of 5 mV s^{-1}, 50 mV s^{-1}, 100 mV s^{-1}, and 300 mV s^{-1}.

Table 10. Specific capacitances of supercapacitors using PETK800(w) and PETK900(w)

	Gravimetric capacitance [F g^{-1}]						Volumetric capacitance [F cm^{-3}]						
Current density [A g^{-1}]	0.1	0.5	1	3	5	7	0.1	0.5	1	3	5	7	R_{ret}[a] [%]
PETK800(w)	23.7	21.6	19.7	12.8	8.6	5.8	23.8	21.8	19.8	12.9	8.6	5.9	24.5
PETK900(w)	20.4	19.9	17.2	14.9	13.1	11.4	17.0	16.6	14.3	12.5	10.9	9.5	55.9

[a]Retention ratio with increasing C-D: calculated from the ratio of specific capacitances at 0.1 and 7 A g^{-1}

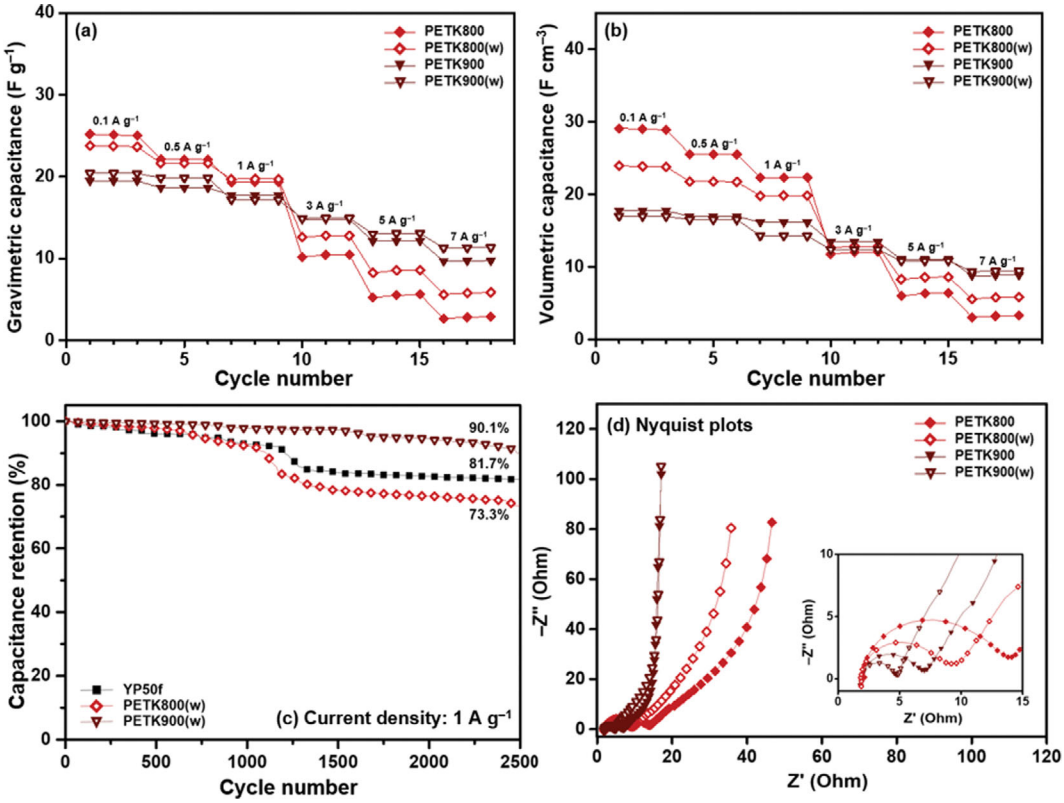

Fig. 13. (a) Gravimetric capacitances, (b) Volumetric capacitances, (c) long-term durability of supercapacitors using YP50f, PETK800(w) and PETK900(w), and (d) electrochemical impedance spectra using PETK800s and PETK900s derived from waste or PET chip.

In addition, we performed C-D measurements at the applied current densities of 0.1, 0.5, 1, 3, 5, and 7 A g^{-1} and similarly used Eqs. (5) and (6) to calculate the specific capacitances. As shown in in Fig. 13(a) and Table 10, the initial C_g and the tendency for the capacitance to decrease with increasing current densities are quite analogous to the CV results. However, the volumetric capacitance of PETK800(w) is lower than that of PETK800 [see Fig. 13(b)] because of the lower loading mass and the different properties of PETK800 and PETK800(w). To confirm their long-term durability, we performed 2500 cycles of C-D analysis at 1 A g^{-1}, and the results are presented in Fig. 13(c). After 2500 cycles, PETK800(w) and PETK900(w) showed long-term durability of 73.3% and 90.1%, which correspond perfectly to those of PETK800 and PETK900, respectively. These results thus confirm that waste PET can be used to produce ACs under the same conditions as we employed for PET chips and that active materials can be obtained from plastic waste with remarkably similar properties to those obtained from PET chips.

5-2. Resistance Properties

To check the electrical resistance properties, we performed EIS analysis, and the results are presented in Fig. 13(d). The diameters of the semicircles show that the values of R_{ct} for PETK800(w) and PETK900(w) are much smaller than those for PETK800 and PETK900, respectively. In addition, the waste PET-derived carbons show low sheet resistance in the FPP results (Table 11). Based on their low resistance properties, high rate capabilities can be expected for PETK800(w) and PETK900(w). According to the characterization results of the ACs derived using each type of PET, the waste PET-derived ACs have the advantage of high electrical conductivity despite their less developed SSAs. Overall, the ACs derived from waste PET and PET chips have similar properties and thus have potential applicability to electrode materials for supercapacitors with the benefit of eco-friendliness.

Table 11. Sheet resistance of PETK800(w) and PETK900(w)

Sample	PETK800(w)	PETK900(w)
R_{sheet} [a] [Ohm $sq.^{-1}$]	473	193

[a]Sheet resistance

CONCLUSIONS

We have described the successful preparation of carbon electrodes for supercapacitors using carbonization and activation of commercially available PET chips. In the activation process, we used either KOH (for chemical activation) or CO_2 (for physical activation) as an activating agent. Based on the drastic increase in the SSA and the development of crystallinity observed in several chemically activated PET-derived carbons (PETKs), we found that chemical activation using KOH is suitable for manufacturing PET-derived ACs. In all the PETKs, we observed large increases in the SSA compared with the SSA of PET800, the carbon material obtained after carbonization. In particular, PETK900 showed the highest

crystallinity, and it had a large SSA of 2076.7 m^2 g^{-1} due to the abundance of micropores, which increases the adsorption of electrolyte ions, and plentiful mesopores, which facilitate ion transfer. Using PETK900 as an active material in a supercapacitor, we verified that a supercapacitor with PETK900 exhibited considerable capacitance and higher long-term durability than YP50f, which is a representative commercial form of AC. Additionally, we produced waste plastic-derived carbons under the same conditions using PET obtained from waste water bottles. We confirmed that PETK800(w) and PETK900(w) also exhibit outstanding electrochemical properties as active materials for supercapacitors based on their large SSAs and adequate pore development. In conclusion, we determined that the carbonization and activation methods reported in this study can be used as a promising approach for the recycling of plastic waste and as a solution to the environmental problems caused by waste plastic.

ACKNOWLEDGEMENTS

This work was supported by the National Research Foundation of Korea (NRF) grant funded by the Korea government (MSIT) (2021R1F1A1046272).

SUPPORTING INFORMATION

Additional information as noted in the text. This information is available via the Internet at http://www.springer.com/chemistry/journal/11814.

REFERENCES

1. E. Frackowiak, Q. Abbas and F. Béguin, *J. Energy Chem.*, **22**, 226 (2013).
2. A. González, E. Goikolea, J. A. Barrena and R. Mysyk, *Renew. Sust. Energy Rev.*, **58**, 1189 (2016).
3. L. Zhang, X. Hu, Z. Wang, F. Sun and D. G. Dorrell, *Renew. Sust. Energy Rev.*, **81**, 1868 (2018).
4. G. Wang, L. Zhang and J. Zhang, *Chem. Soc. Rev.*, **41**, 797 (2012).
5. T. Sato, S. Marukane, T. Morinaga, T. Kamijo, H. Arafune and Y. Tsujii, *J. Power Sources*, **295**, 108 (2015).
6. G. G. Prasad, N. Shetty, S. Thakur, Rakshitha and K. B. Bommegowda, *Mater. Sci. Eng.*, **561**, 012105 (2019).
7. M. Ciszewski, A. Koszorek, T. Radko, P. Szatkowski and D. Janas, *J. Electron. Mater.*, **48**, 717 (2019).
8. Z. Yu, L. Tetard, L. Zhai and J. Thomas, *Energy Environ. Sci.*, **8**, 702 (2015).
9. E. Frackowiak and F. Béguin, *Carbon*, **39**, 937 (2001).
10. P. Simon and Y. Gogotsi, *Nat. Mater.*, **7**, 845 (2008).
11. T. V. Pham, J.-G. Kim, J. Y. Jung, J. H. Kim, H. Cho, T. H. Seo, H. Lee, N. D. Kim and M. J. Kim, *Adv. Funct. Mater.*, **29**, 1905511 (2019).
12. D. Gastol, J. Walkowiak, K. Fic and E. Frackowiak, *J. Power Sources*, **326**, 587 (2016).
13. N. Jäckel, D. Weingarth, M. Zeiger, M. Aslan, I. Grobelsek and V. Presser, *J. Power Sources*, **272**, 1122 (2014).
14. Z. Zhu, S. Tang, J. Yuan, X. Qin, Y. Deng, R. Qu and G. M. Haarberg, *Int. J. Eletrochem. Sci.*, **11**, 8270 (2016).
15. M. Aslan, D. Weingarth, N. Jäckel, J. S. Atchison, I. Grobelsek and V. Presser, *J. Power Sources*, **266**, 374 (2016).
16. S. Ajit, S. Palaniappan and S. Gopukumar, *Synth. Met.*, **180**, 43 (2013).
17. C. Bauer, A. Bilican, S. Braxmeier, G. Reichenauer and A. Krueger, *Carbon*, **197**, 555 (2022).
18. G. Yang, T. Takei, Y. Zhu, E. Iranmanesh, B. Liu, Z. Li, J. Wang, P. Hiralal, G. A. J. Amaratunga, O. Fontaine and H. Zhou, *Electrochim. Acta*, **397**, 139242 (2021).
19. N. Jäckel, D. Weingarth, A. Schreiber, B. Krüner, M. Zeiger, A. Tolosa, M. Aslan and V. Presser, *Electrochim. Acta*, **191**, 284 (2016).
20. Y. Hamano, S. Tsujimura, O. Shirai and K. Kano, *Mater. Lett.*, **128**, 191 (2014).
21. S. J. Taylor, M. D. Haw, J. Sefcilk and A. J. Fletcher, *Langmuir*, **30**, 10231 (2014).
22. F. N. Ajjan, M. Vagin, T. Rębiś, L. E. Aguirre, L. Ouyang and O. Inganäs, *Adv. Sustainable Syst.*, **1**, 1700054 (2017).
23. Z. Liu, S. Liu, R. Dong, S. Yang, H. Lu, A. Narita, X. Feng and K. Müllen, *Small*, **13**, 1603388 (2017).
24. P. Ratajczak, M. E. Suss, F. Kaasik and F. Béguin, *Energy Storage Mater.*, **16**, 126 (2019).
25. J. Choi, I. Yang, S.-S. Kim, S. Y. Cho and S. Lee, *Macromol. Rapid Commun.*, **43**, 2100467 (2021).
26. I. Yang, S.-G. Kim, S. H. Kwon, M.-S. Kim and J. C. Jung, *Electrochim. Acta*, **223**, 21 (2017).
27. J.-A. Kim, I.-S. Park, J.-H. Seo and J.-J. Lee, *Trans. Electr. Electron. Mater.*, **15**, 81 (2014).
28. F. Xu, Y. Qiu, G, Jiang, B. Ding, J. Li, Q. Liu, J. Wu, X. Xu, H. Wang and Y. Liang, *Macromol. Rapid Commun.*, **40**, 1800770 (2019).
29. Y. Liu, P. Liu, Lin, Li, S. Wang, Z. Pan, C. Song and T. Wang, *J. Electroanal. Chem.*, **903**, 115828 (2021).
30. M. Jung, I. Yang, J. Yoo, M.-S. Kim and J. C. Jung, *J. Electrochem. Soc.*, **168**, 080532 (2021).
31. I. Yang, J. Yoo, J. Lee, M.-S. Kim and J. C. Jung, *J. Electrochem. Soc.*, **166**, A3950 (2019).
32. D. R. Lobato-Peralta, R. Amaro, D. M. Arias, A. K. Cuentas-Gallegos, O. A. Jaramillo-Quintero, P. J. Sebastian and P. U. Okoye, *J. Electroanal. Chem.*, **901**, 115777 (2021).
33. X. Yuan, M.-K. Cho, J. G. Lee, S. W. Choi and K. B. Lee, *Environ. Pollut.*, **265**, 114868 (2020).
34. C. Yuwen, B. Liu, Q. Rong, L. Zhang and S. Guo, *Sci. Total Environ.*, **817**, 152995 (2022).
35. S. Sharifian and N. Asasian-Kolur, *J. Anal. Appl. Pyrolysis*, **163**, 105496 (2022).
36. I. Yang, J. H. Mok, M. Jung, J. Yoo, M.-S. Kim, D. Choi and J. C. Jung, *Macromol. Rapid. Commun.*, **43**, 2200006 (2022).
37. S. Chen, Z. Liu, S. Jiang and H. Hou, *Sci. Total Environ.*, **710**, 136250 (2020).
38. M. Karakoti, S. Pandey, R. Jangra, P. S. Dhapola, P. K. Singh, S. Mahendia, A. Abbas and N. G. Sahoo, *Mater. Manuf.*, **36**, 171 (2021).
39. E. Azwar, W. A. W. Mahari, J. H. Chuah, D.-V. N. Vo, N. L. Ma, W. H. Lam and S. S. Lam, *Int. J. Hydrog. Energy*, **43**, 20811 (2018).
40. K. R. Vanapalli, H. B. Sharma, V. P. Ranjan, B. Samal, J. Bhattacharya, B. K. Dubey and S. Goel, *Sci. Total Environ.*, **750**, 141514 (2021).
41. K. S. Khoo, L. Y. Ho, H. R. Lim, H. Y. Leong and K. W. Chew, *J. Hazard. Mater.*, **417**, 126108 (2021).

42. J. Huang, A. Veksha, W. P. Chan, A. Giannis and G. Lisak, *Renew. Sust. Energ. Rev.*, **154**, 111866 (2022).
43. A. L. P. Silva, J. C. Prata, T. R. Walker, A. C. Duarte, W. Ouyang, D. Barcelò and T. Rocha-Santos, *Chem. Eng. J.*, **405**, 126683 (2021).
44. S. Brunauer, P. H. Emmett and E. Teller, *J. Am. Chem. Soc.*, **60**, 309 (1938).
45. I. Yang, D. Kwon, M.-S. Kim and J. C. Jung, *Carbon*, **132**, 503 (2018).
46. I. Yang, M. Jung, M.-S. Kim, D. Choi and J. C. Jung, *J. Mater. Chem. A*, **9**, 9815 (2021).
47. J. Yoo, I. Yang, D. Kwon, M. Jung, M.-S. Kim and J. C. Jung, *Energy Technol.*, **9**, 2000918 (2021).
48. D.-W. Kim, H.-S. Kil, K. Nakabayashi, S.-H. Yoon and J. Miyawaki, *Carbon*, **114**, 98 (2017).
49. K. László, A. Bóta and I. Dékány, *Carbon*, **41**, 1205 (2003).
50. A. C. Ferrari and J. Robertson, *Phys. Rev. B*, **61**, 14095 (2000).
51. A. C. Ferrari, *Solid State Commun.*, **143**, 47 (2007).
52. F. Tuinstra and J. L. Koenig, *J. Chem. Phys.*, **53**, 1126 (1970).
53. D. Qu and H. Shi, *J. Power Sources*, **74**, 99 (1998).
54. H. D. Yoo, J. H. Jang, J. H. Ryu, Y. Park and S. M. Oh, *J. Power Sources*, **267**, 411 (2014).
55. C. Lei, F. Markoulidis, Z. Ashitaka and C. Lekakou, *Electrochim. Acta*, **92**, 183 (2021).
56. C. Portet, P. L. Taberna, P. Simon and C. Laberty-Robert, *Electrochim. Acta*, **49**, 905 (2004).
57. B.-A. Mei, O. Munteshari, J. Lau, B. Dunn and L. Pilon, *J. Phys. Chem. C*, **122**, 194 (2018).
58. X. Liu, L. Juan, L. Zhan, L. Tang, Y. Wang, W. Qiao, X. Liang and L. Ling, *J. Electroanal. Chem.*, **642**, 75 (2010).